This is the peer-reviewed, final accepted version for American Mineralogist, published by the Mineralogical Society of America.
The published version is subject to change. Cite as Authors (Year) Title. American Mineralogist, in press.
DOI: https://doi.org/10.2138/am-2021-7838. http://www.minsocam.org/

REVISION 1

Mn^{3+} AND THE PINK COLOR OF GEM-QUALITY EUCLASE FROM NORTHEAST BRAZIL

Lætitia Gilles-Guéry[1], Laurence Galoisy[1,*], Jurgen Schnellrath[2], Benoit Baptiste[1], Georges Calas[1]

[1] Sorbonne Université, Muséum National d'Histoire Naturelle, CNRS, IRD, Institut de Minéralogie, de Physique des Matériaux et de Cosmochimie (IMPMC), 4 Place Jussieu 75252 Paris Cedex 05 Paris, France

[2] Centro de Tecnologia Mineral (CETEM), Ilha da Cidade Universitária, 21.941-908 Rio de Janeiro, RJ, Brazil

* *Corresponding author : Laurence Galoisy , Sorbonne Université, IMPMC, BC 115, 4 place Jussieu 75005 Paris, France. laurence.galoisy@sorbonne-universite.fr*

ABSTRACT

Pink euclase of gem-quality and centimeter size, presenting an unusual pink-orange coloration and a pink to orange pleochroism, has been discovered near Livramento de Nossa Senhora, in Bahia State, Brazil. The origin of the pink coloration has been investigated using different spectroscopic techniques: UV-Vis-NIR spectroscopy, Electron Paramagnetic Resonance (EPR), luminescence and X-ray Absorption Near Edge Structure (XANES). The coloration is mainly due

to the presence of Mn^{3+} substituted to octahedral Al^{3+} that causes an intense split band at about 18500 and 21000 cm^{-1}. The crystal field splitting $10D_q$, Crystal Field Stabilization Energy (CFSE) and Racah parameter B for Mn^{3+} are 2055.5 cm^{-1}, 147 kJ/mol, and 886 cm^{-1}, respectively. The Mn^{3+} molar extinction coefficient varies as a function of polarization, between 23 and 55 $L.mol^{-1}.cm^{-1}$. An additional absorption band, occurring near 24000 cm^{-1}, together with the rising background towards the UV, tentatively assigned to the $O \rightarrow Fe^{3+}$ OMCT contribute to the pink-orange hue. The UV-Vis-NIR *in situ* spectra during the heating treatment (up to 500°C) show a color change toward an intense stable pink color. CIE colorimetric parameters demonstrate that the color of the investigated euclase remains in the pink domain before and after heat treatment. In the absence of Mn^{2+}, shown by EPR and luminescence, the presence of Mn^{3+} evidences oxidative formation conditions due to a contamination of the hydrothermal fluids by the surrounding host rock.

Keywords : euclase, manganese, pink color, optical spectroscopy, crystal field, heat treatment, pleochroism, gems.

INTRODUCTION

Euclase ($BeAlSiO_4(OH)$) is a nominally colorless monoclinic nesosilicate mineral (space group $P2_1/c$). It is an unusual gem, recognized for its ornamental qualities and of interest to gem and mineral collectors, though its perfect cleavage parallel to (010) makes it generally unsuitable for use in jewelry. The first specimen of euclase was found near Ouro Preto, brought to Europe in 1785 by Joseph Dombey and described and named by René-Just Haüy, from the greek words "eu" and "klasis" meaning "well-breaking" (Atencio, 2015). It is encountered as euhedral crystals in various hydrothermal contexts and granitic pegmatites

(Cerny, 2002; Simmons et al., 2012). Despite it often occurs as well-formed crystals, euclase has an inconspicuous appearance, forming small crystals, easily overlooked within pegmatitic mineral assemblages. It is usually a breakdown product of beryl in low temperature (200 - 400°C), acidic (pH 4-5) hydrothermal fluids, at high alumina activity or associated in secondary assemblages with quartz and kaolinite (Cerny, 2002).

The structure of euclase consists of distorted $BeO_3(OH)$ tetrahedra and regular SiO_4 tetrahedra linked by corner-sharing along the *c*-axis. These tetrahedra are interconnected with slightly distorted $AlO_5(OH)$ octahedra by corner sharing through hydroxyl groups, which form zigzag chains by edge sharing also along the c-axis (Hazen et al., 1986). The Al-O distances range from 1.851 to 1.983 Å with O-Al-O angles from 79.8 to 99.3 (Supplemental Figure S1a). The shortest octahedral O-O distance corresponds to the shared edge between Al octahedra. The average Al-O distance in euclase (1.902 Å, standard deviation of 0.050) is typical of octahedral Al^{3+} in regular sites, as observed in beryl and grossular with 6 Al-O distances at 1.91 and 1.92 Å, respectively. This average distance is also similar to that in moderately distorted sites in corundum (1.914 Å, standard deviation of 0.064) (Hazen et al., 1986). The smaller standard deviation shows that the octahedral Al site is slightly less distorted in euclase than in corundum. The zigzag chains can be described by an alternation of Al-Al pairs with d(Al-Al) = 2.84 and 2.94 Å. The shorter Al-Al distance is along the r direction, which forms a 10° angle with the c-axis (Supplemental Figure S1b). Each oxygen atom is three-coordinated, receiving a formal Pauling bond strength sum of 2.0.

Euclase is often colorless but may also be blue-, green- and yellow-colored, sometimes presenting a color zoning. The 6-coordinated Al site may accommodate Cr or Fe impurities, responsible for the diversity of euclase colors. The green color arises from the presence of

Cr^{3+} (Krambrock et al., 2008). Fe-substitution in the Al-site is at the origin of a Fe^{2+}-Fe^{3+} charge-transfer absorption band (IVCT), responsible for an intense blue color (Mattson and Rossman, 1987). By contrast, pink euclase is very rare. A few small crystals of pale pink euclase, millimeter size, have been reported in the Borborema Pegmatitic Province, Brazil (Eeckhout et al., 2002; Cassedanne and Philippo, 2015). Pale pink euclase has also been recently extracted for collector purpose at the Brumado pit, Bahia state, Brazil (https ://www.mindat.org/loc-192235.html). However, the origin of this pink coloration is unknown.

Though Mn^{3+} has a limited stability field in aqueous solutions, as a result of a disproportionation into Mn^{2+} and Mn^{4+}, it is stabilized in about 30 minerals, either trapped during crystal growth or as a result of external irradiation (see e.g. Laurs et al., 2003; Kurtz et al., 2020). It is an efficient coloring impurity in minerals (Burns, 1993). As a $3d^4$ ion, Mn^{3+} is subject to a Jahn-Teller effect that stabilizes it in distorted sites. In the case of a substitution of Al^{3+} by Mn^{3+}, the octahedral site is expected to undergo a distortion because of the difference of ionic radii [$r(Al^{3+})$ = 0.535 Å vs. $r(Mn^{3+})$ = 0.645 Å (Burns, 1993)].

This work reports the first investigation of euclase crystals, several centimeters large, with a pink-orange coloration (Supplemental Figure S2). The samples were recently discovered in NE Brazil, near Livramento de Nossa Senhora, Bahia State, close to the Chapada Diamantina National Park. Their euhedral shape and their association with euhedral quartz indicate a formation in a hydrothermal context. Located at 70 km of the above-mentioned Brumado pit, the Livramento de Nossa Senhora deposit is known for its resources in gem-quality varieties of colored and colorless hydrothermal quartz (Reys, 2017). The original euclase coloration, with a pink to orange pleochroism, originates from octahedral Mn^{3+} substituted to Al^{3+}. An additional contribution to pleochroism is due to a combination of a band at 24000 cm^{-1} and of

a rising absorption edge, tentatively assigned to the $O \rightarrow Fe^{3+}$ Oxygen to Metal Charge Transfer (OMCT). Heating from 300°C to 500°C in air during 3h retains the initial intensity of the Mn^{3+} absorption bands and results in the annealing of the 24000 cm^{-1} contribution and a drastic decrease of the intensity of the OMCT. This induces a stable intense pink coloration. The presence of Mn^{3+} in the absence of Mn^{2+} is consistent with oxidizing formation conditions (Tarantola et al., 2019).

EXPERIMENTAL

The chemical composition has been determined using a CAMECA SX-100 electron microprobe analysis (EMPA) at the Camparis platform, Sorbonne Université, Paris, France. The analyses have been averaged over 100 analytical points. The standard minerals that were used for the analysis are diopside (Si$K\alpha$), orthoclase (Al$K\alpha$), $MnTiO_3$ (Ti$K\alpha$; Mn$K\alpha$), Fe_2O_3 (Fe$K\alpha$), pure Ge (Ge$K\alpha$). A 25 kV, 10 nA beam current counting 5 s was used for the Al, Si, Ge elements. A 25 kV, 200 nA beam current counting 30 s was used for Ti, Mn, Fe elements. Corrections were made using the usual PAP procedure (CAMECA). BeO and H_2O, which cannot be quantified using the electron microprobe, have been obtained by difference.

The crystallographic parameters (a = 4.6309 Å, b = 14.3312 Å, c = 4.7769 Å, β = 100.295° in the $P2_1$/c space group) were determined using a XCalibur S 4-circle diffractometer equipped with a Sapphire CCD detector. The euclase single crystal was oriented along the A and B orientations, (crystal sections (001) and (010), respectively), using x-ray diffraction. Crystal thickness was determined by means of a digital Mitutoyo micrometer with an accuracy of ± 1 µm. The E//a, E//b, E//c, E⊥c and E//r polarization directions were recorded (Hålenius and Skogby, 1996), using a Glan Taylor polarizer made of two calcite prisms.

Optical absorption spectra of pristine euclase and the sample heated at 500°C and recovered at ambient temperature have been obtained in transmission mode in the 330 - 2000 nm (5000 - 30000 cm^{-1}) range with a resolution of 1 nm using a Perkin Elmer Lambda 1050 UV/Vis/NIR Spectrometer (IMPMC, spectroscopy platform) with a 4×4 mm beam size. A He-cryostat under vacuum (around 3.4×10^{-7} mbar) attached to the spectrometer, was used to record low temperature spectra (down to 10K). The sample was not damaged when coming back to room temperature. In situ high temperature optical spectra of the sample have been recorded up to 500°C in air, with steps of 50°C lasting 30 min using a Linkam heating stage which needs to be held horizontal and thus combined with a Cassegrain-type microscope with a beam size of 20 - 150 µm diameter (Chassé et al., 2015). Fits of the obtained spectra were carried out using the Fityk software (Wojdyr, 2010), under the assumption of a Gaussian line shape for both *d-d* absorption bands and the UV-absorption edge. Colorimetric *Yxy* coordinates were computerized from the measured unpolarized optical spectra using the CIE 1931 convention and the D_{65} illuminant (average midday light in Western Europe) published by the CIE (Hunt, 1991).

Electronic Paramagnetic Resonance (EPR) spectrum has been recorded using a X-band Bruker EMX-plus spectrometer operating at 9.86 GHz. The spectrum of the powered sample was obtained from 0 to 4000 G at room temperature with a 100 kHz frequency modulation, 1.002×10^{2} mW microwave power, and 1.00 T modulation amplitude. The magnetic field range was calibrated relative to a DPPH standard ($g = 2.0037 \pm 0.0002$).

X-ray Absorption Near Edge Structure (XANES) spectra at the Fe K-edge were measured on the LUCIA beamline at the SOLEIL synchrotron (Saint-Aubin, France) with a Si(311) monochromator (Vantelon et al., 2016). The storage ring was operating in top-up mode at an

137 electron current of 450 mA and 2.57 GeV. Polarized XANES spectra have been recorded on
138 single crystals (E//*c*) at ambient temperature with fluorescence detection. The XANES spectra
139 are recorded on the 7075 – 7300 eV range with 0.1 eV steps for the pre-edge (0.2 eV steps for
140 the other XANES regions) and a 150 ms counting time. XANES spectra were collected using
141 the continuous flyscan mode. A possible drift of the pre-edge features was checked to ensure
142 the absence of irradiation effects with a good accuracy of the data.
143
144
145 ## RESULTS & DISCUSSION
146
147 ### Chemical composition and redox state
148 The chemical composition is close to the stoichiometric formula with 33.22 vs. 35.14 wt.%
149 Al_2O_3 and 43.09 wt.% vs. 41.41 wt.% SiO_2, respectively. Such a limited variability was
150 already reported (Pignatelli et al., 2017). However, the sum $\Sigma(Al_2O_3 + SiO_2)$ remains close to
151 the theoretical value, with 76.31 wt.% vs. 76.55 wt.%, respectively.
152 The minor and trace elements detected by EMPA are Fe, Mn, Ti and Ge. The average Fe
153 content is 992 ppm. It is similar to that in blue and colorless euclase from Northeast Brazil
154 (Graziani and Guidi, 1980; Guedes et al., 2006). The average Mn content is 73 ppm. A similar
155 content, 150 ppm, has been found in pink beryls from Minas Gerais, Brazil (Blak et al., 1982).
156 The average Ti content is 46 ppm. It may be pointed out that Mn and Ti are unusual in euclase
157 and have not been detected in colorless or greenish-blue samples from other locations
158 (Graziani and Guidi, 1980; Pignatelli et al., 2017). Finally, the sample contains an unusual
159 concentration of Ge, 142 ppm, more than one order of magnitude above the average

concentration in pegmatites and quartz-topaz greisens (Bernstein, 1985; Höll et al., 2007; Breiter et al., 2013). Trace elements found in euclase samples from other localities (Sharp, 1961; Graziani and Guidi, 1980; Hanson, 1985), such as Na, K, Ca, Sc, Cu or Sn, were not detected.

As for the other euclase crystals investigated (Dias et al., 2009), the powder EPR spectrum of our pink euclase does not present native paramagnetic radiation-induced defects. This spectrum (Supplemental Figure S3) presents only a signal from Fe^{3+}, substituted in the slightly distorted Al^{3+} octahedral site, corresponding to the EPR spectra of single crystals of blue and colorless euclase (Guedes et al., 2006) in which some Fe^{3+} has been evidenced. The absence of the EPR signals of Mn^{2+} and Ti^{3+} indicates that Mn and Ti occur as Mn^{3+} and Ti^{4+}, respectively. Moreover, the luminescence of Mn^{2+} has been tested under UV lamp. No Mn^{2+} luminescence has been detected neither under short nor long wavelengths. The excitation with red (785nm) or green laser (532 nm) did not show laser-induced luminescence. This confirms the absence of Mn^{2+} in the pink euclase investigated.

XANES spectra were recorded at the Fe K-edge. Special care was given to avoid radiation-induced artifacts on Fe-speciation (see Experimental Section). They were compared to crystalline references representing typical Fe-speciation: siderite ($FeCO_3$) for $^{VI}Fe^{2+}$, staurolite ($Fe_2Al_9Si_4O_{23}$ (OH)) for $^{VI}Fe^{2+}$, andradite ($Ca_3Fe_2Si_3O_{12}$) for $^{VI}Fe^{3+}$ and Fe-berlinite ($FePO_4$) for $^{IV}Fe^{2+}$ (Supplemental Figure S4). The energy position and low intensity of the pre-edge evidences the only presence of Fe^{3+} in octahedral coordination. XANES data indicate that the heating treatment at 500°C does not change the redox state of iron, which remains in the ferric state.

Optical absorption spectra and the pink – orange pleochroism

The polarized spectra (E//a, E//b, E//c) present two narrow bands at 7000 and 10200 cm^{-1} corresponding to the first and second overtones of the OH stretching mode (Fig. 1). Curve fitted spectra in the visible range show two main bands corresponding to the $^5E_g \rightarrow {}^5T_{2g}$ transition of Mn^{3+}, with the splitting of the $^5T_{2g}$ level due to the low symmetry field, in which Mn^{3+} is usually stabilized by a Jahn Teller effect (Burns, 1993). The corresponding transitions will be referred to as v_1 and v_2, respectively. The v_1 band is located at 18465 cm^{-1}, 18453 cm^{-1} and 18780 cm-1 for E//a, E//b and E//c, respectively. The v_2 band occurs at 21246 cm^{-1}, 21449 cm^{-1} and 21000 cm^{-1} for E//a, E//b and E//c, respectively. The characteristics of the v_1 and v_2 bands are given in Table 1. Weak bands near 20000-23000 cm^{-1} are related to Mn^{3+} spin-forbidden transitions. The small features at 23680, 26250 and 27610 cm^{-1} are assigned to Fe^{3+} spin-forbidden transitions, from $^6A_1(S)$ to ^4E,$^4A_1(^4G)$, $^4T_{2g}(^4D)$ and $^4E_g(^4D)$, respectively (Burns, 1993; Vercamer et al., 2015). This is consistent with the presence of substitutional Fe^{3+} in the octahedral sites of Al^{3+} as shown by the EPR powder spectrum of our sample and XANES measurements (Supplemental Figures S3 and S4). The absence of crystal field transitions of Fe^{2+}, expected at 8000 and 11600 cm^{-1} in euclase (Mattson and Rossman, 1987), also indicates that iron only occurs as Fe^{3+}. The spectra show a strong UV absorption edge with a low-energy tail that rapidly falls off towards the visible range. It may arise from light scattering by optical heterogeneities (inclusions and fractures) and to the $O \rightarrow Fe^{3+}$ OMCT simulated by a Gaussian function centered at 40000 cm^{-1}. This value is close to that determined in other studies as e.g. planetary materials and glasses (Cloutis et al., 2008; Vercamer et al., 2015).

Unpolarized optical spectra of the pink euclase in the A and B orientations, crystal section (001) and (010) respectively, are presented on Fig. 2. The difference in position of the main Mn^{3+} bands is at the origin of the orange to pink pleochroism (Supplemental Figure S5). The simultaneous pink and orange hues lead to the typical pink-orange coloration of euclase. The orange hue is related to the rising slope in the UV domain combined with an additional absorption at 24000 cm^{-1}. The combination of the two transmission windows in the red and violet domains results in the pink coloration. As these two transmission windows are wider in the B orientation than in the A orientation, the pink coloration is more intense in the B orientation, leading to the observed pleochroism.

To quantify the color and the pleochroism of the investigated euclase, the chromatic coordinates were calculated using unpolarized optical spectra in order to describe the color as observed with naked eye (Fig. 3). The coordinates are overlaid onto the CIE (Commission Internationale de l'Eclairage) 1931 color space template, and give the chromaticity (hue and saturation) of the color. The horse-shoe shape defines all visible colors. In its center, the white reference point enables the assessment of the color saturation, especially for thin samples. The colorimetric coordinates of euclase in the A and B orientations indicate a variation of color from orange to pink resulting from the pleochroism of the crystal. On Fig. 3, The comparison with another pleochroic Mn^{3+}-bearing mineral, pezzottaite (Rossman, 2021), shows a distinct pleochroism from pink-orange to pinkish purple, illustrating the original coloration of pink-orange euclase.

Crystal chemistry of Mn^{3+}

This is the peer-reviewed, final accepted version for American Mineralogist, published by the Mineralogical Society of America.
The published version is subject to change. Cite as Authors (Year) Title. American Mineralogist, in press.
DOI: https://doi.org/10.2138/am-2021-7838. http://www.minsocam.org/

228

229 The ν_1 and ν_2 transitions of Mn^{3+} in euclase, at around 18500 and 21000 cm^{-1}, occur at a similar
230 position as in grossular (17302 and 19504 cm^{1}: Geiger et al., 1999), beryl (17900 and 20000 cm^{-1}
231 : Czaja et al., 2018) or corundum (18750 and 20600 cm^{1}: McClure, 1962). The splitting of the
232 upper $^5T_{2g}$ term, related to site distortion, remains smaller in these minerals, 1850 to 2500 cm^{-1},
233 relative to the larger vales observed in other minerals as viridine or piemontite, 14100 and 12000
234 cm^{-1}, respectively (Burns, 1993).

235 The five Mn^{3+} spin-forbidden transitions are well-resolved at 10 K (Fig. 2). According to
236 the d^4 Tanabe-Sugano diagram, the transition at 19500 cm^{-1} corresponds to the octahedral
237 Mn^{3+} field-independent transition $^5B_1(D) \rightarrow {}^3E(H)$. The other transitions at 20700, 21125,
238 22375 and 23125 cm^{-1} also arise from transitions to field independent levels derived from the
239 ^3H, ^3F and ^3G states of octahedral Mn^{3+}, as observed in kyanite (Wildner et al., 2013), red
240 beryl (Czaja et al., 2018; Fridrichová et al., 2018) or elbaite tourmaline (Kurtz et al., 2020).

241 Using the barycenter calculation method, D_q parameter is calculated to be 2055 cm^{-1}. This
242 value is among the highest recorded in Mn^{3+}-bearing minerals. The spin-forbidden, field
243 independent $^5B_1(D) \rightarrow {}^3E(H)$ transition at 19500 cm^{-1} provides a way to calculate the Racah
244 parameter B = 886 cm^{-1}. This value is intermediate between that in corundum, 965 cm^{-1}
245 (McClure, 1962), and in beryl, 818-835 cm^{-1} (Czaja et al., 2018; Fridrichová et al., 2018)
246 showing a variation in the covalent contribution of the Mn^{3+}-O bond in these minerals.

247 The Crystal Field Stabilization Energy (CFSE) for Mn^{3+} ions increases with the distortion
248 of the site (Burns, 1993; Hålenius et al., 2004). The small CFSE value in euclase, 147 kJ/mol,
249 is similar to the 130 - 152 kJ/mol values found for octahedral Mn^{3+} in beryl, corundum, garnet
250 or diopside, showing a slight distortion of the Mn^{3+} site (McClure, 1962; Hålenius et al., 2004;

Czaja et al., 2018). Higher CFSE values of 185-200 kJ/mol reflect more distorted sites in andalusite, epidote and tetragonal garnets (Abs-Wurmbach et al., 1981; Hålenius and Skogby, 1996; Hålenius et al., 2004).

The EPR data show the absence of Mn^{2+}, thus, the molar extinction coefficient ε was directly calculated from the intensity of the Mn^{3+} absorption bands. The value of ε (Mn^{3+}) (Table 2) is similar to that found in hydrogarnets (5 - 50 $L.mol^{-1}.cm^{-1}$; Hålenius, 2004). As the removal of the center of symmetry relaxes the Laporte selection rule, ε increases with the distortion of the Mn^{3+} site (Smith et al., 1982), the values observed in euclase in the directions E//*a*, E//*b*, E//*c*, E⊥*c* (23 - 38 $L.mol^{-1}.cm^{-1}$) confirm a moderate distortion. The higher molar extinction coefficient value (~51 $L.mol^{-1}.cm^{-1}$) in the *r* direction may be explained by a coupled substitution of Mn^{3+} in both octahedral adjacent Al^{3+} sites inducing a stronger distortion of the sites.

After isochronal heating from 300 to 500°C, the color changes to pure pink (Fig. 4). This modification of the color is also visible using the chromatic coordinates between 300°C (pink-orange) and 500°C (pure pink) (Fig. 3). The fit of the polarized optical spectra recorded at ambient temperature on the pristine sample indicates the presence of a Gaussian component around 24000 cm^{-1} (Fig. 1). This component disappears after heating at 500°C (Fig. 5). At the same time, the rising background towards the UV domain falls down. As a consequence, the transmission window between 23000 and 25000 cm^{-1} is enlarged, the orange hue disappears and the color of the crystal turns pure pink. This 24000 cm^{-1} band, with a larger width than the v_1 and v_2 bands whatever the polarization, shows an intensification in the E//*b* direction (Table

272 1). As no signal related to paramagnetic defect centers can be observed on the EPR spectrum,
273 this thermally unstable band may be tentatively attributed to diamagnetic defects.
274

275 ## IMPLICATIONS

276 The absence of Mn^{2+} in the euclase investigated precludes a radiation-enhanced Mn-
277 oxidation, often observed in other Mn^{3+}-bearing minerals and easily annealed at 350°C giving
278 colorless minerals (Laurs et al., 2003; Kurtz et al., 2020). Therefore, a stable pink color due to
279 the presence of Mn^{3+} implies oxidative formation conditions. The euclase crystals occur in a
280 hydrothermal vein hosted in a schist. Local oxidizing conditions are illustrated by the
281 presence of abundant large green andalusite (viridine) crystals, in the schist (Supplemental
282 Figure S6), a well-known Mn^{3+} mineral (Hålenius, 1978; Smith et al., 1982; Schnellrath,
283 1989; Abs-Wurmbach et al., 2001). At a regional scale, epidote group minerals, hosting Mn^{3+},
284 and sericite are associated to plagioclase in the basement that includes the Brumado pluton
285 (Teixeira et al., 2010). In the Brumado pluton, the Pedra Preta magnesite deposit also shows
286 the presence of epidote, together with lepidolite (Bodenlos, 1954). The Brumado pit has been
287 recently reported to host pink euclase (https ://www.mindat.org/loc-192235.html). As shown
288 for the conditions of formation of gems in Rhodope (Tarantola et al., 2019), this may lead to
289 the preservation of an oxidizing environment during the migration of the fluids in the São
290 Francisco craton. A low fluid/rock ratio during the whole geodynamic evolution and a Fe-
291 poor character of the hydrothermal fluid are necessary to buffer the oxygen activity to high
292 levels and create adequate oxidizing conditions. These parameters have been invoked to
293 explain the formation of Mn^{3+} bearing gems (Tarantola et al., 2019) among which pink
294 tourmaline (Laurs et al., 1998). In the present case, this will preserve the presence of Mn^{3+}

295 during the contamination of hydrothermal fluids by the surrounding rocks, as suggested by the
296 high Ge content of the sample.
297 Indeed, the pink euclase investigated presents an unusual high Ge concentration, 142 ppm.
298 Germanium has also been detected in blue and colorless euclase from Minas Gerais, Brazil
299 (Graziani and Guidi, 1980) and, locally, a concentration of 97-105 ppm Ge was found in
300 andalusite from Paramirim das Crioulas, located 20 km from Livramento de Nossa Senhora
301 (Schnellrath, 1989). This may indicate a contamination of the hydrothermal fluids, by analogy
302 with Colombian euclase, which presents also high Ge contents (230 - 530 ppm: Pignatelli et
303 al., 2017), an indirect indication of the contamination of the hydrothermal fluids by the
304 surrounding host rock. An implication of these peculiar formation conditions is that redox
305 conditions appear to govern the color of euclase. EPR and luminescence indicate the absence
306 of Mn^{2+}. As shown by XANES, pink euclase contains iron only in the ferric form. By
307 contrast, in blue euclase, the presence of Fe^{2+}, involved in a characteristic Fe^{2+}- Fe^{3+} IVCT in
308 this mineral, indicates more reducing conditions. This makes euclase color an interesting
309 indicator of the formation conditions.
310 Among pink colored gemstones (topaz, tourmaline, garnets, beryls…), the newly discovered
311 pink-orange euclase presents unusual hue and pleochroism that make it particularly attractive
312 for collectors. The heat-treatment modifies the color from pink-orange to a stable pure pink
313 coloration. In tourmaline, the heating treatment results in almost all absorption features being
314 lost, resulting in a colorless mineral. By contrast, in euclase, the Mn^{3+} absorption bands follow
315 being observed in heated samples resulting in a stable pure pink coloration.
316
317

ACKNOWLEDGMENTS

The IMPMC X-ray diffraction and spectroscopy platforms and the Sorbonne Université – Camparis microprobe facility are acknowledged for their technical support. The authors thank Maxime Guillaumet for his invaluable help during spectroscopic measurements and two anonymous reviewers for their helpful comments.

REFERENCES CITED

Abs-Wurmbach, I., Langer, K., Seifert, F., and Tillmanns, E. (1981) The crystal chemistry of (Mn^{3+},Fe^{3+})-substituted andalusites (viridines and kanonaite) ($Al_{1-x-y}Mn^{3+}_xFe^{3+}_y)_2(O/SiO_4$) : crystal structure refinements, Mössbauer and polarized optical absorption spectra. Zeitschrift für Kristallographie, 155, 81 - 113.

Atencio, D. (2015) The discovery of new mineral species and type minerals from Brazil. Brazilian. Journal of Geology, 45, 143 - 158.

Bernstein, L.R. (1985) Germanium geochemistry and mineralogy. Geochimica et Cosmochimica Acta, 49, 2409 - 2422.

Blak, A.R., Isotani, S., and Watanabe, S. (1982) Optical absorption and Electron Paramagnetic Resonance studies of colorless and pink beryl. Revista Brasileira de Fisica, 12, 285 - 292.

Bodenlos, A.J. (1954) Magnesite deposits in the Serra das Eguas, Brumado Bahia, Brazil. U.S. Geol. Surv. Bull., 975‑C, Washington, D. C.

Breiter, K., Gardenová, N., Kanický, V., Vaculovič, T. (2013) Gallium and germanium geochemistry during magmatic fractionation and post-magmatic alteration in different types of granitoids: A case study from the Bohemian Massif (Czech Republic). Geologica Carpathica, 64, 171-180.

Burns, R.G. (1993) Mineralogical Applications of Crystal Field Theory. Cambridge University Press, seconde edition.

Cassedanne, J., and Philippo, S. (2015) Mineral and gem deposits of eastern Brazilian pegmatites, volume 1 & 2. Luxembourg, Musée National d'Histoire Naturelle edition.

348 Cerny, P. (2002) Mineralogy of Beryllium in Granitic Pegmatites. Reviews in Mineralogy
349 and Geochemistry, 50, 405 - 444.
350 Chassé, M., Lelong, G., van Nijnatten, P., Schoofs, I., de Wolf, J., Galoisy, L., and Calas,
351 G. (2015) Optical Absorption Microspectroscopy (μ-OAS) Based on Schwarzschild-Type
352 Cassegrain Optics. Applied Spectroscopy, 69, 457 - 463.
353 Cloutis, E., Mccormack, K., Belliii, J., Hendrix, A., Bailey, D., Craig, M., Mertzman, S.,
354 Robinson, M., and Riner, M. (2008) Ultraviolet spectral reflectance properties of common
355 planetary minerals. Icarus, 197, 321 - 347.
356 Czaja, M., Lisiecki, R., Chrobak, A., Sitko, R., and Mazurak, Z. (2018) The absorption-
357 and luminescence spectra of Mn^{3+} in beryl and vesuvianite. Physics and Chemistry of
358 Minerals, 45, 475 - 488.
359 Dias, L.N., Pinheiro, M.V.B., and Krambrock, K. (2009) Radiation-induced defects in
360 euclase : formation of O^{-} hole and Ti^{3+} electron centers. Physics and Chemistry of Minerals,
361 36, 519 - 525.
362 Eeckhout, S.G., Castañeda, C., Ferreira, A.C.M., Sabioni, A., De Grave, E., and
363 Vasconcelos, D.C.L. (2002) Spectroscopic studies of spessartine from Brazilian pegmatites.
364 American Mineralogist, 87, 1297–1306.
365 Fridrichová, J., Bačík, P., Ertl, A., Wildner, M., Dekan, J., and Miglierini, M. (2018) Jahn-
366 teller distortion of Mn^{3+}-occupied octahedra in red beryl from Utah indicated by optical
367 spectroscopy. Journal of Molecular Structure, 1152, 79 - 86.
368 Geiger, C.A., Stahl, A., Rossman, G.R. (1999) Raspberry-red grossular from Sierra de
369 Cruces Range, Coahuila, Mexico. European Journal of Mineralogy, 11, 1109–1113.

Graziani, G., and Guidi, G. (1980) Euclase from Santa do Encoberto, Minais Gerais, Brazil. American Mineralogist, 65, 183 - 187.

Guedes, K. J., Krambrock, K., Pinheiro, M.V.B., and Menezes Filho, L. A. D. (2006) Natural iron-containing blue and colorless euclase studied by electron paramagnetic resonance. Physics and Chemistry of Minerals, 33, 553 - 557.

Hanson, A. (1985) Découverte d'euclase dans le filon de quartz à Ottré, massif de Stavelot, Belgique. Bulletin de Minéralogie, 108, 139 - 143.

Hazen, R.M., Au, A.Y., and Finger, L.W. (1986) High-pressure crystal chemistry of beryl ($Be_3Al_2Si_6O_{18}$) and euclase ($BeAlSiO_4OH$). American Mineralogist, 71, 977 - 984.

Höll, R., Kling, M., Schroll, E. (2007) Metallogenesis of germanium—a review. Ore Geology Reviews, 30, 145-180.

Hunt, R.W.D. (1991) Measuring colour. Wiley edition, Chichester, United Kindom.

Hålenius, U. (1978) A spectroscopic investigation of manganian andalusite. Canadian Mineralogist, 16, 567 - 575.

Hålenius, U., and Skogby, H. (1996) Crystal field spectra of trivalent manganese in synthetic and natural (Na^{+}-Mn^{3+})-substituted diopside. European Journal of Mineralogy, 8, 1231 - 1240.

Hålenius, U. (2004) Stabilization of trivalent Mn in natural tetragonal hydrogarnets on the join 'hydrogrossular'—henritermierite, $Ca_3Mn_2^{3+}[SiO_4]_2[H_4O_4]$. Mineralogical Magazine, 68, 335 - 341.

Krambrock, K., Guedes, K.J., and Pinheiro, M.V.B. (2008) Chromium and vanadium impurities in natural green euclase and their relation to the color. Physics and Chemistry of Minerals, 35, 409 - 415.

Kurtz, D.A., Rossman, G.R., and Hunter, B.M. (2020) The Nature of the Mn(III) Color Centers in Elbaite Tourmalines. Inorganic Chemistry, 59, 9618 - 9626.

Laurs, B.M., Dilles, J.H., Wairrach, Y., Kausar, A.B., and Snee, L.W. (1998) Geological setting and petrogenesis of symmetrically zoned, miarolitic granitic pegmatites at Stak Nala, Nanga Parbat - Haramosh massif, Northern Pakistan. Canadian Mineralogist, 36, 1- 47.

Laurs, B.M., Simmons, W.B., Rossman, G.R., Quinn, E.P., McClure, S.F., Peretti, A., Armbruster, T., Hawthorne, F.C., Falster, A.U., Günther, D., Cooper, M.A., Grobéty, B. (2003) Pezzottaite from Ambatovita, Madagascar: a new gem mineral. Gems and Gemology,, 39, 284–301.

Mattson, S.M., and Rossman, G.R. (1987) Identifying characteristics of charge transfer transitions in minerals. Physics and Chemistry of Minerals, 14, 94 - 99.

McClure, D.S. (1962) Optical spectra of transition-metal ions in corundum. Journal of Chemical Physics, 36, 2757 - 2779.

Pignatelli, I., Giuliani, G., Morlot, C., Rouer, O., Claiser, N., Chatagnier, P.Y., and Goubert, D. (2017) Recent advances in understanding the similarities and differences of Colombian euclase samples. Canadian Mineralogist, 55, 799 - 820.

Reys, A. (2017) Coloured Stone Mining and Trade in Brazil: A Brief History and Current Status. Journal of Gemmology, 35, 708 - 726.

Rossman, G.R. (2021) Mineral Spectroscopy Server Published: 2021 Publisher: California Institute of Technology. URL: http://minerals.gps.caltech.edu/index.html

Schnellrath, J. (1989) Brasilianische Andalusite und Zink-Staurolithe von EdelsteinQualität : Chemismus, Bildungsbedingungen, optische und kristallographische Eigenschaften. PhD thesis, Johannes Gutenberg-Universität, Mainz.

Sharp, W.N. (1961) Euclase in greisen pipes and associated deposits, Park county, Colorado. American Mineralogist, 46, 1505 - 1508.

Simmons, W.B., Pezzotta, F., Shigley, J.E., and Beurlen, H. (2012) Granitic Pegmatites as Sources of Colored Gemstones. Elements, 8, 281 - 287.

Smith, G., Hålenius, U., and Langer, K. (1982) Low temperature spectral studies of Mn^{3+}bearing andalusite and epidote type minerals in the range 30000-5000 cm^{-1}. Physics and Chemistry of Minerals, 8, 136 - 142.

Tarantola, A., Voudouris, P., Eglinger, E., Scheffer, C., Trebus, K., Bitte, M., Rondeau, B., Mavrogonatos, C., Graham, I., Etienne, M., and Peiffert, C. (2019) Metamorphic and Metasomatic Kyanite Bearing Mineral Assemblages of Thassos Island (Rhodope, Greece). Minerals, 9, 252.

Teixeira, J.B.G., da Glória da Silva, M., Misi, A., Cerqueira Pereira Cruz, S., and da Silva Sá, J.H. (2010) Geotectonic setting and metallogeny of the northern São Francisco craton, Bahia, Brazil. Journal of South American Earth Sciences, 30, 71-83.

Vantelon, D., Trcera, N., Roy, D., Moreno, T., Mailly, D., Guillet,S., Metchalkov, E., Delmotte, F., Lassalle, B., Lagarde, P. and Flank, A-M. (2016) The Lucia beamline at SOLEIL. Journal of Synchrotron Radiation, 23, 635-640

Vercamer, V., Lelong, G., Hijiya, H., Kondo, Y., Galoisy, L., and Calas, G. (2015) Diluted Fe^{3+} in silicate glasses: Structural effects of Fe-redox state and matrix composition. An optical absorption and X-band/Q-band EPR study. Journal of Non-Crystalline Solids, 428, 138 - 145.

Wildner, M., Beran, A., and Koller, F. (2013) Spectroscopic characterisation and crystal field calculations of varicoloured kyanites from Loliondo, Tanzania. Mineralogy and Petrology, 107, 289 - 310.

439 Wojdyr, M. (2010) Fityk : a general-purpose peak fitting program. Journal of Applied

440 Crystallography, 43, 1126 - 1128.

441

Figure Captions

Figure 1: a) Polarized optical spectra of pink-orange euclase along the *a*, *b* and *c*-axes. b) Example of curve resolved polarized optical spectrum of euclase along the *a*-axis. The red curve is the experimental spectrum after subtracting the tail of the Gaussian-shaped UV absorption edge at 45000 cm^{-1} for the OMCT $O \rightarrow Fe^{3+}$. The black plain curves are the nine fitted Gaussian contributions: two major components (18465 cm^{-1}; 21246 cm^{-1}), six minor components (19916 cm^{-1}; 20300 cm^{-1}; 20668 cm^{-1}; 22420 cm^{-1}; 23100 cm^{-1}; 23665 cm^{-1}) and one component at 23630 cm^{-1}. The black dotted curve is the sum of the fitted components.

Figure 2: Unpolarized optical spectra of pink-orange euclase in the A orientation and B orientation (crystal sections (001) and (010), respectively) and at 10K in the A orientation with (*s-f*) the spin-forbidden transitions of Mn^{3+} and Fe^{3+} in octahedral site.

Figure 3: Colorimetric representation of the pleochroism (in black) and the heat treatment effects (in red) of the pink euclase in the CIE color space chromaticity diagram (calculated from 380 to 780 nm optical spectra system *Yxy* with D_{65}) by comparison with the chromaticity values (in green) of pezzottaite (after the data of Rossman, 2021).

Figure 4: Optical microspectroscopic study of the isochronal in situ measurements between 300°c and 500°C of pink euclase in the B orientation.

Figure 5: Curve resolved unpolarized optical spectrum at ambient temperature of euclase in the B direction after heat treatment (500°C). The red curve is the experimental spectrum after

This is the peer-reviewed, final accepted version for American Mineralogist, published by the Mineralogical Society of America.
The published version is subject to change. Cite as Authors (Year) Title. American Mineralogist, in press.
DOI: https://doi.org/10.2138/am-2021-7838. http://www.minsocam.org/

subtracting a Gaussian baseline for the UV domain for the OMCT $O \rightarrow Fe^{3+}$. The black plain curves are the fitted Gaussian contributions: two major components for the Mn^{3+} spin-allowed (*s*-*a*) transitions (18784 cm^{-1}; 20983 cm^{-1}) and five minor components for Mn^{3+} spin-forbidden (*s*-*f*) transitions (19900 cm^{-1}; 20356 cm^{-1}; 20737 cm^{-1}; 22515 cm^{-1}; 23151 cm^{-1}) and three minor components for Fe^{3+} spin-forbidden (*s*-*f*) transitions (23758 cm^{-1}; 26276 cm^{-1}; 27615 cm^{-1}). The black dotted curve is the sum of the fitted components.

Table 1: Position (v), molar extinction coefficient (ε), width ($\omega_{1/2}$) and splitting magnitude of resolved Mn^{3+} spin-allowed transitions in polarized spectra of the pink euclase.

Parameters	E // *a*	E // *b*	E // *c*	E ⊥ *c*	E // *r*
v_1 (cm^{-1})	18465	18453	18780	18804	18963
ε ($L.mol^{-1}.cm^{-1}$)	25.84	23.01	38.21	34.52	55.53
$\omega_{1/2}$ (cm^{-1})	2400	3200	2600	2400	2500
v_2 (cm^{-1})	21246	21449	21000	21085	21000
ε ($L.mol^{-1}.cm^{-1}$)	33.11	27.28	30.66	29.17	28.47
$\omega_{1/2}$ (cm^{-1})	2400	3000	2600	2400	2400
Splitting (cm^{-1})	2781	2996	2220	2281	2097

This is the peer-reviewed, final accepted version for American Mineralogist, published by the Mineralogical Society of America.
The published version is subject to change. Cite as Authors (Year) Title. American Mineralogist, in press.
DOI: https://doi.org/10.2138/am-2021-7838. http://www.minsocam.org/

479

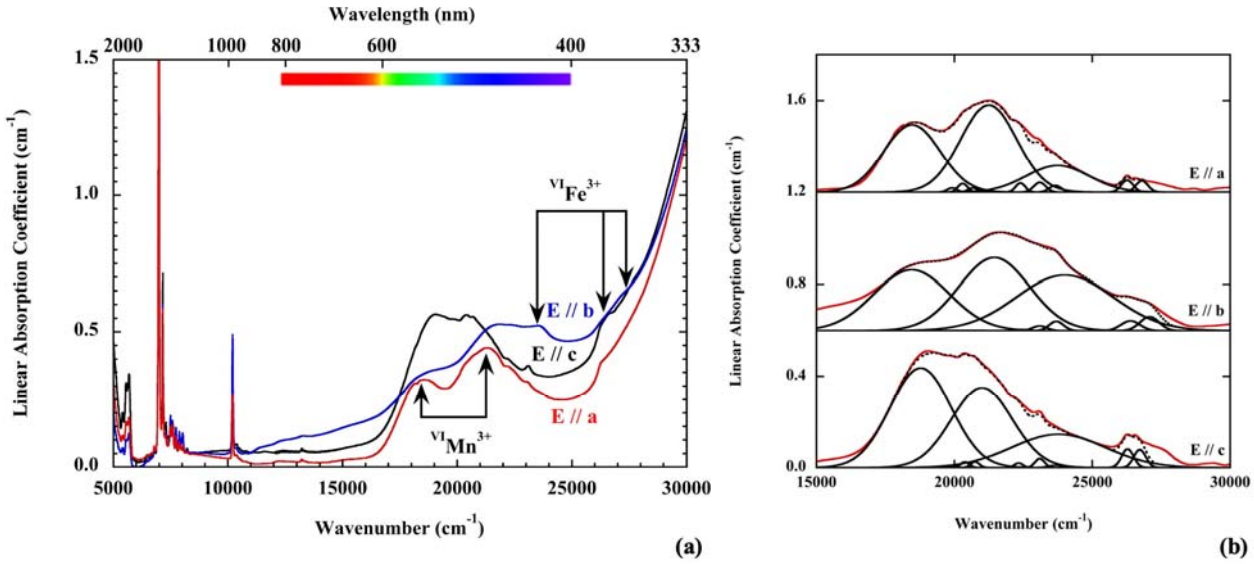

480
481 Figure 1
482

This is the peer-reviewed, final accepted version for American Mineralogist, published by the Mineralogical Society of America.
The published version is subject to change. Cite as Authors (Year) Title. American Mineralogist, in press.
DOI: https://doi.org/10.2138/am-2021-7838. http://www.minsocam.org/

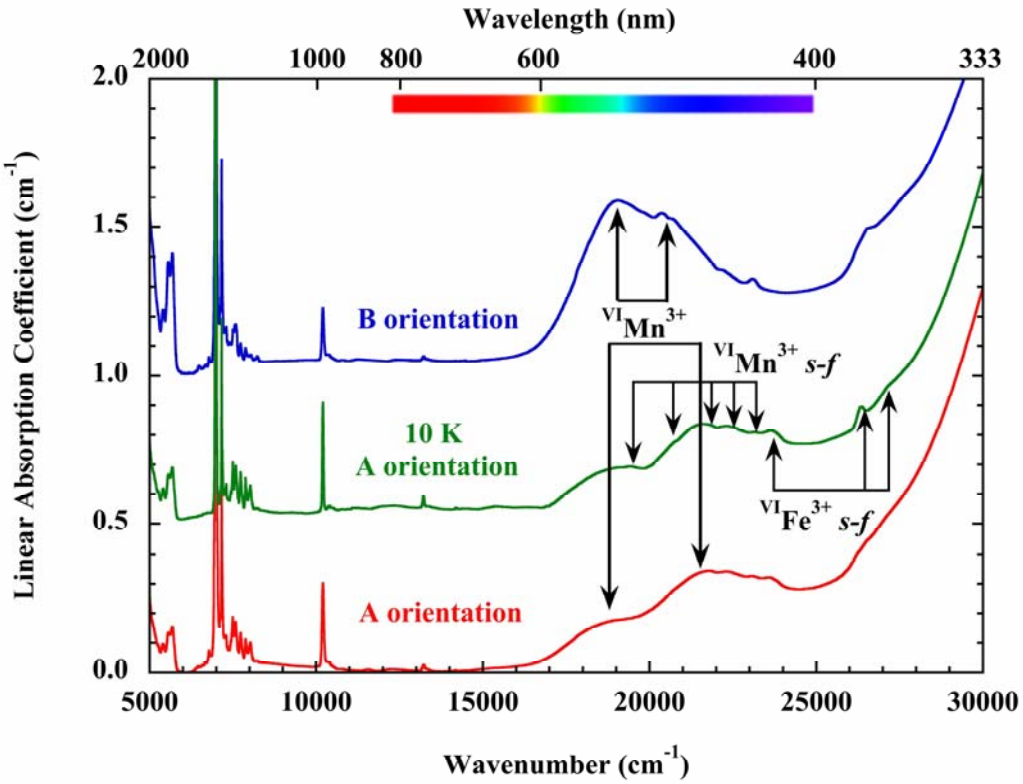

Figure 2

This is the peer-reviewed, final accepted version for American Mineralogist, published by the Mineralogical Society of America.
The published version is subject to change. Cite as Authors (Year) Title. American Mineralogist, in press.
DOI: https://doi.org/10.2138/am-2021-7838. http://www.minsocam.org/

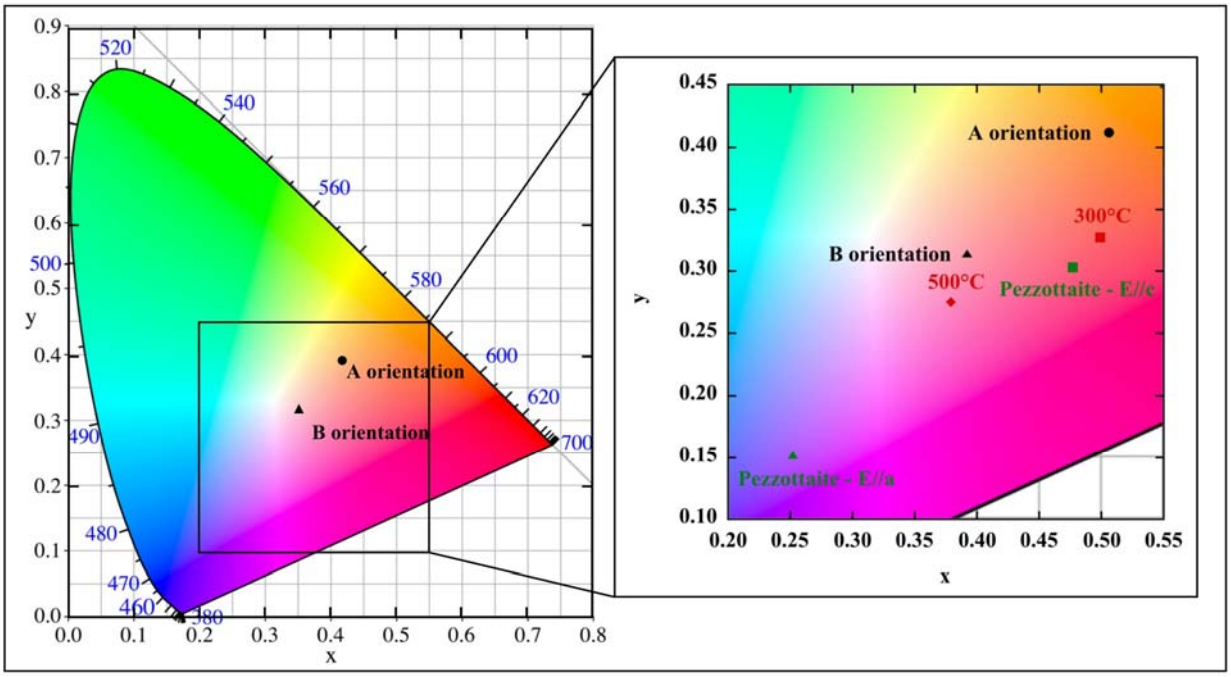

Figure 3

This is the peer-reviewed, final accepted version for American Mineralogist, published by the Mineralogical Society of America.
The published version is subject to change. Cite as Authors (Year) Title. American Mineralogist, in press.
DOI: https://doi.org/10.2138/am-2021-7838. http://www.minsocam.org/

490

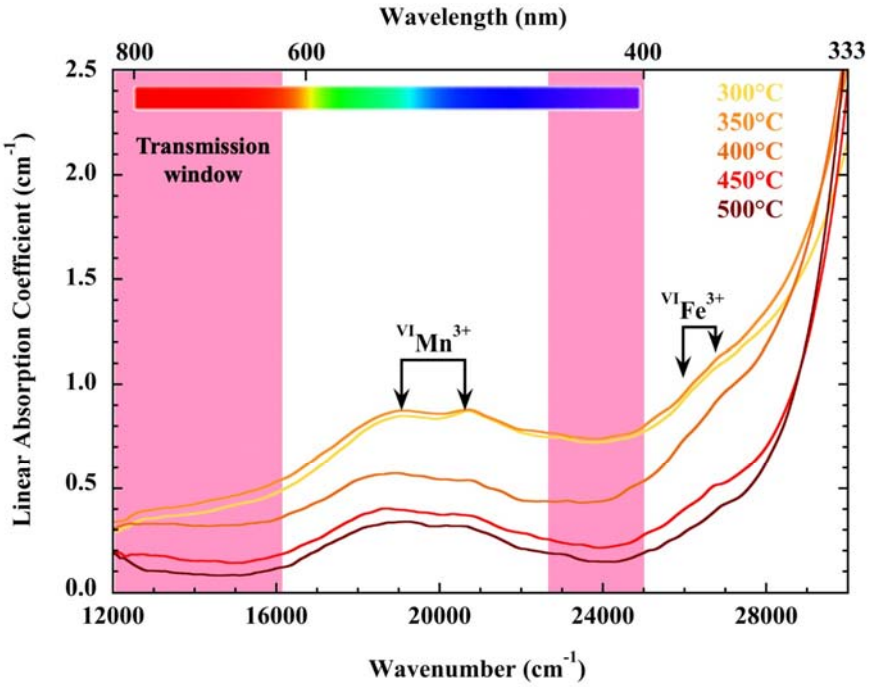

491
492 Figure 4
493

This is the peer-reviewed, final accepted version for American Mineralogist, published by the Mineralogical Society of America.
The published version is subject to change. Cite as Authors (Year) Title. American Mineralogist, in press.
DOI: https://doi.org/10.2138/am-2021-7838. http://www.minsocam.org/

494

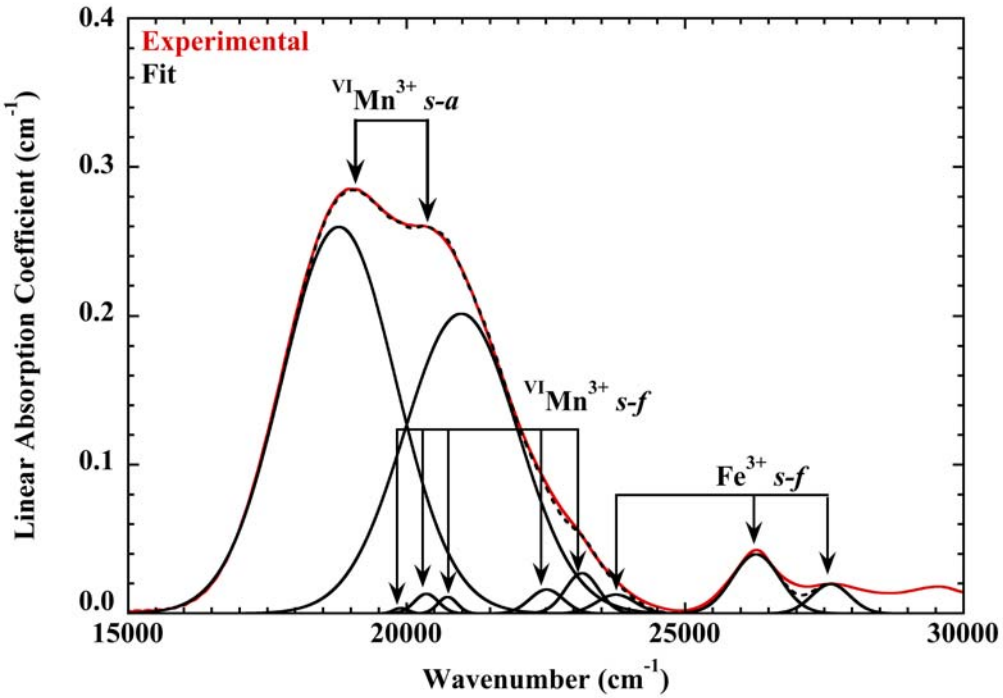

495
496 Figure 5